



Ceria modified FeMnO_x—Enhanced performance and sulphur resistance for low-temperature SCR of NO_x



Liam John France^a, Qing Yang^a, Wan Li^a, Zhihang Chen^{b,*}, Jianyu Guang^a, Dawei Guo^c, Lefu Wang^a, Xuehui Li^{a,*}

^a School of Chemistry and Chemical Engineering, Pulp & Paper Engineering State Key Laboratory of China, South China University of Technology, Guangzhou, 510640, PR China

^b Guangdong Key Laboratory of Water and Air Pollution Control, South China Institute of Environmental Science, Ministry of Environmental Protection, Guangzhou, 510655, PR China

^c Research Institute of Petroleum Processing Sinopec, Beijing, 100083, PR China

ARTICLE INFO

Article history:

Received 22 August 2016

Received in revised form

21 December 2016

Accepted 5 January 2017

Available online 12 January 2017

Keywords:

FeMnO_x

CeO₂

Low-temperature SCR

Sulphur resistance

Fast-SCR

ABSTRACT

Low-temperature NH₃-SCR is an environmentally important reaction for the abatement of NO_x from stationary sources. In recent years FeMnO_x has attracted significant attention as a potential catalyst for this process, however its catalytic activity and SO₂ resistance require further improvement. In this contribution FeMnO_x has been modified to examine the effect of ceria on catalytic activity and SO₂ resistance in the low temperature region. Preparation of catalysts via the citric acid method generate modified materials that exhibit enhanced NO turnover compared to FeMnO_x. A reduction in NH₃ adsorption (NH₃-TPD) and a suitable ratio between NO sites (NO-TPD) and chemisorbed surface oxygen (XPS) are beneficial for the promotion of fast-SCR. A comparative SO₂ resistance study of FeMnO_x and Ce(12.5) showed that the latter exhibited improved stability in the presence of SO₂, as indicated by the retention of pore volume (N₂ adsorption) and surface composition (XPS). *In-situ* DRIFTS demonstrated that chemisorbed N-containing species on Ce(12.5) were much more stable in the presence of SO₂ compared to FeMnO_x, which resulted in the formation of significantly less metal sulphates and NH₄HSO₄.

Crown Copyright © 2017 Published by Elsevier B.V. All rights reserved.

1. Introduction

Nitrogen oxides NO_x (mainly in the form NO and NO₂) emitted from both stationary (fossil-fueled power plants or FCC units) and mobile sources (gasoline or diesel engines) pose serious environmental problems such as acid rain, photochemical smog, ozone depletion, the greenhouse effect etc. Selective catalytic reduction (SCR) with ammonia is considered the most useful commercialised approach for NO_x removal from stationary sources in view of economic and technological efficiency. In recent years, low-temperature SCR catalysts capable of working under conditions at the back-end of the exhaust system have attracted much interest due to their excellent performance and durability [1–8]. However, small concentrations of SO₂ still remain in the flue gas after the electrostatic precipitator (ESP) and desulphurisation devices. SO₂ can further react with NH₃ and O₂ to generate sulphates, which deposit on the surface of the catalyst and cause pore plugging. Of more

serious concern is the chemisorption of SO_x on the transition metal deNO_x catalyst, which are unable to desorb at low temperature resulting in the eventual deactivation of the catalyst via sulphation [9–14]. Preventing or reducing these modes of catalyst deactivation in the low temperature regime is of great interest both industrially and academically for SCR catalysts. Tang et al. found that Fe and V doping into AC/C supported MnO_x-based monolithic catalysts could improve both low-temperature SCR activity and SO₂ resistance [15]. Kang et al. reported that manganese oxides containing small amounts of copper oxide with a high surface area is the most active catalyst for low temperature NO reduction with NH₃ in the presence of SO₂ [16]. The promotional effect of copper oxide was found to coincide with the formation of the Cu-Mn spinel CuMn₂O₄, NO could be oxidised into NO₂ easily via electronic transfer between copper and manganese. Wu et al. found resistance to SO₂ could be significantly enhanced over the Mn/TiO₂ via doping with Ce [17], its addition prevented the formation of Ti(SO₄)₂ and Mn(SO₄)₂ and significantly inhibited the deposition of (NH₄)₂SO₄ and NH₄HSO₄. Ke et al. demonstrated that sulphation of active sites on the metal oxide (Co₃O₄), resulted in enhanced sulphur resistance within the range of their study [18]. But, no unanimous conclu-

* Corresponding authors.

E-mail addresses: chenzhihang@scies.org (Z. Chen), cexhli@scut.edu.cn (X. Li).

sions on the mechanism of this enhancement effect can be drawn at present. Kobayashi et al. studied the reactivity and sulphur tolerance of V_2O_5 catalysts supported on TiO_2 - SiO_2 - MoO_3 (TSM) in low-temperature SCR [6]. The observed enhancement of sulphur tolerance is attributed to significantly reduced SO_2 oxidation activity of the V_2O_5 /(TSM) catalyst, which was ascribed to its increased acidity. Notoya et al. reported that SO_2 was not a poison to TiO_2 and ZrO_2 based catalysts for low-temperature SCR [19], their proposed mechanism suggested that SO_2 contributes to the production of active surface oxygen. This active oxygen was thought to interact with surface NO_{ad} and form NO_{2ad} , this species could further react with NH_4^{+ad} generating NH_4NO_{2ad} , which would preferentially decompose to N_2 , H_2O , and a small amount of NO.

A number of previous studies have examined the activity of bimetallic Mn-based mixed oxides [20,21]. $Cr(0.4)$ - MnO_x prepared by the citric acid method resulted in NO_x conversions in excess of 98.5% at 120 °C with a GHSV of 30,000 h⁻¹. This significant activity was attributed to the formation of the $CrMn_{1.5}O_4$ phase, which was found to decrease the reduction temperature of manganese oxides [20]. A series of $FeMnO_x$ catalysts prepared by the citric acid method were examined at 100 °C with a GHSV of 30,000 h⁻¹, it was found that the most active catalyst was $Fe(0.4)Mn(0.6)O_x$, yielding a NO_x conversion of 98% with 100% N_2 selectivity. XRD patterns revealed that this high activity occurred in conjunction with the formation of a new crystalline phase, $Fe_3Mn_3O_8$ [21].

As a non-toxic material, CeO_2 is potentially advantageous for a wide variety of catalytic applications. It can promote structure stability and improve catalytic activity, besides which, oxygen can be stored and released via the redox shift between Ce^{4+} and Ce^{3+} , thus the oxidation of NO to NO_2 may be promoted and redox properties may be enhanced [22–25]. CeO_2 has been widely used in catalytic applications, especially SCR to remove NO_x [26–28], however, its application as a low level additive has seldom been explored in this capacity. This study examines a series of CeO_x doped $FeMnO_x$ materials for their effectiveness in the removal of NO_x , resistance to SO_2 , H_2O and their combination at low temperature. The observed results for activity and sulphur resistance are further rationalised via the use of a number of different characterisation techniques, to examine physiochemical properties of the surface and bulk structures.

2. Experimental

2.1. Catalyst preparation

Manganese acetate (99.0%), ferric nitrate (98.5%), ceria (where applicable) and 2 mol L⁻¹ citric acid (99.5%), where the citric acid to metal ion is 1, were mixed under vigorous stirring at room temperature for 1 h and dried at 120 °C for 12 h. The molar ratio of Mn: Fe was set at 3:2 in this contribution as it was found to be the optimal value previously [21]. The resulting porous, foam-like solid was calcined at 500 °C for 3 h under air in a muffle furnace, after which the resulting catalysts were pressed and sieved to 60–100 mesh and denoted as $Ce(y)$, where y is the molar percentage value of CeO_x .

2.2. NO_x SCR activity and SO_2 resistance

NO_x SCR activity measurements were carried out in a fixed-bed quartz tube reactor (13 mm i.d. and 430 mm length) with an internal thermocouple to monitor catalyst bed temperature, approximately 2.6 g of catalyst (60–100 mesh) was used for each experiment. The simulated flue gas consisted of, 0.1% NO, 0.1% NH_3 , 3% O_2 , (0.01% SO_2 , 5% or 10% H_2O when used) and a balance of N_2 , 860 mL min⁻¹ total flow rate (under ambient conditions) was employed to generate a GHSV of approximately 30,000 h⁻¹. Com-

position of the feed gas and effluent stream were continuously monitored using online sensors with emission monitors (SWG-300, MRU, Germany) for analysis of NO, NO_2 , and O_2 . The effluent stream was also analysed via online gas chromatography (4890D, HP, USA), utilising a Porapak Q column to examine the formation of N_2O and a 0.5 nm molecular sieve column for N_2 . To avoid errors caused by oxidation of ammonia in the converter of the NO_x analyser, an ammonia trap-containing a phosphoric acid solution was installed before the sample inlet to the flue gas analyser. For SO_2 , H_2O and combined SO_2 / H_2O resistance experiments the SCR reaction was allowed to stabilise for 2 h at 120 °C, generating steady-state conditions prior to introducing SO_2 , H_2O or their combination into the flue gas. Steady-state NO_x conversion (1), specific activity (2) and activity (3) were calculated according to the following equations;

$$C(NO_x) = \frac{\varphi(NO_x)_{in} - \varphi(NO_x)_{out}}{\varphi(NO_x)_{in}} \times 100\% \quad (1)$$

$$\text{Specific activity} = \frac{\left(\frac{(\varphi(NO_x)_{in} \times T_f)}{(60 \times 24,000)}\right) \times \left(\frac{(\varphi(NO_x)_{in} - \varphi(NO_x)_{out})}{\varphi(NO_x)_{in}}\right)}{(S_A \times 2.6)} \quad (2)$$

$$\text{Activity} = \left(\frac{(\varphi(NO_x)_{in} \times T_f)}{(60 \times 24,000)}\right) \times \left(\frac{(\varphi(NO_x)_{in} - \varphi(NO_x)_{out})}{\varphi(NO_x)_{in}}\right) \times N_A \quad (3)$$

$\varphi(NO_x) = \varphi(NO) + \varphi(NO_2)$, and the subscripts *in* and *out* indicate the inlet concentration and outlet concentration at steady state respectively. Specific activity expressed in nmol s⁻¹ m⁻², where T_f is the total flow rate in mL min⁻¹, 60 is the number of seconds in a minute, 24,000 mL is the volume occupied by a mole of gas at 25 °C and atmospheric pressure and S_A is the specific surface area in m² g⁻¹. Activity is defined by the units s⁻¹, N_A is Avogadro's constant.

Sulphur contaminated catalysts were collected after 4 h SCR reaction in the presence of 100 ppm SO_2 . The SO_2 -containing flue gas was stopped and nitrogen was flowed over the spent catalyst to remove physisorbed species while cooling the reaction to room temperature, at this point the catalyst was removed and stored for further analysis. They are denoted as $FeMnO_x$ -S and $Ce(12.5)$ -S, where S indicates the use of SO_2 for 4 h, unless otherwise stated. Multiple experiments have been conducted on all catalysts to determine the error associated with the catalytic data, it has been found that the data varies by a maximum of 2% across 5 variable temperature experiments for each catalyst.

2.3. Catalyst characterisation

X-ray diffraction (XRD) patterns were obtained using a Rigaku D/MAX-3A Auto X-ray diffractometer with Cu K α radiation ($\lambda = 1.5418 \text{ \AA}$). Intensity data were collected over a 2 θ range of 5–85° with a 0.05° step size and an accumulation time of 1 s per step. The XRD phases were identified in comparison with referenced data from the International Centre for Diffraction Data (ICDD) files.

A Micromeritics ASAP 2010 micropore-size analyser was used to measure N_2 adsorption isotherms of the samples at liquid N_2 temperature (−196 °C). The specific surface area was determined from the linear portion of the BET plot, pore-size distribution was calculated from the desorption branch of the N_2 adsorption isotherm using the BJH formula. Prior to surface area and pore-size distribution measurements, all samples were degassed in vacuum at 300 °C for 6 h.

The morphology of the catalysts were measured on a JSM-7401F high resolution field emission scanning electron microscope, at a resolution of 1.5 nm, an accelerating voltage of 0.1–30 kV, an electric current of 10^{-13} – 10^{-9} A and a magnification of 25– 10^6 times.

Spectra were collected with a Horiba Jobin Yvon Lab Tam HR Raman spectrometer equipped with an Olympus BX-41 micro-

scope (objective $\times 100$) and a TE-cooled CCD detector (Andor) in a backscattering configuration utilising a He-Ne laser (632.8 nm excitation line) at a power of 5–20 mV with a spectral resolution of 0.8 cm^{-1} .

Temperature-programmed reduction (TPR) was performed on a Micromeritics Auto Chem 2920 chemisorption analyser. 30 mL min^{-1} (NTP) of 10% H_2 in Ar passed over about 100 mg of sample in a quartz reactor. The heating rate was set at $8\text{ }^{\circ}\text{C min}^{-1}$ from 25 to $950\text{ }^{\circ}\text{C}$ for all samples.

NH_3 -, NO - and SO_2 -temperature-programmed desorption (TPD) experiments were performed to determine adsorption/desorption characteristics of each species over the catalyst. 50 mg of each catalyst was loaded in the reactor and was pre-treated in He (30 mL min^{-1}) at $200\text{ }^{\circ}\text{C}$ for 30 min, then cooled to room temperature in the same stream. The pre-treated sample was then exposed to NH_3 (2.45%), NO (2.47%) or SO_2 (0.01%) at a flow rate of 20 mL min^{-1} for 30 min. Physisorbed $\text{NH}_3/\text{NO}/\text{SO}_2$ was removed by flushing the catalysts with He at a flow rate of 30 mL min^{-1} for 30 min at $120\text{ }^{\circ}\text{C}$ prior to TPD. Samples underwent TPD in He (30 mL min^{-1}) from 100 to $950\text{ }^{\circ}\text{C}$ at a heating rate of $10\text{ }^{\circ}\text{C min}^{-1}$.

X-ray photoelectron spectroscopy (XPS) was performed using a Quantum-2000 Scanning ESCA Microprobe (Physical Electronics) with a hemispherical detector operating at constant pass energy ($PE = 46.95\text{ eV}$). An X-ray source at 210 W ($I = 15\text{ mA}$, $U = 14\text{ kV}$) and Al K α radiation (1486.6 eV) were used. Sample powders were pelletized with a diameter of 0.2 mm and tested at $20\text{ }^{\circ}\text{C}$, intensity was determined from the integration of each peak after smoothing and subtraction of the L-shaped background. Binding energies were calculated with reference to the C 1 s peak of contaminant carbon at 284.6 eV with a precision of 0.3 eV. Characteristic peaks were separated utilising peak fitting which was performed using a combination of Gaussian-Lorentzian curves with linear background subtraction. S, C and N counts have not been quantified in this study, total surface concentration is corrected to reflect Ce, Mn, Fe and O only.

In-situ diffuse reflectance infrared Fourier transform spectroscopy (*in-situ* DRIFTS) was performed on a FTIR spectrometer (Bruker Vertex 70) equipped with a smart collector and a MCT/A detector cooled by liquid N_2 . The reaction temperature was controlled precisely via a Pike programmable temperature controller. Prior to each experiment, the sample was pre-treated at $400\text{ }^{\circ}\text{C}$ for 2 h in 150 mL min^{-1} N_2 and cooled to $120\text{ }^{\circ}\text{C}$. The background spectrum was collected in flowing N_2 and automatically subtracted from the sample spectrum. The reaction conditions were controlled as follows, 150 mL min^{-1} total flow rate; 0.1% NH_3 , 0.1% NO , 3% O_2 , (100 ppm SO_2 when used) with a N_2 balance. All spectra were recorded by accumulating 64 scans with a resolution of 4 cm^{-1} .

3. Results and discussion

3.1. Low temperature SCR activity of $\text{Ce}(y)$ catalysts

The performances of FeMnO_x and $\text{Ce}(y)$ catalysts prepared by the citrate method were examined in the SCR of NO_x with NH_3 in the presence of excess O_2 (Fig. 1). FeMnO_x exhibited well defined conversion at relatively high GHSV ($30,000\text{ h}^{-1}$). Considering the results obtained at $75\text{ }^{\circ}\text{C}$ (Fig. 1) it is apparent that the conversion effectively went through a maximum as a function of CeO_x level. In this instance 12.5% resulted in the highest conversion of 72%, however, it must be noted that 5–10% doping levels resulted in similar conversion (approximately 63%). At 15% CeO_x the conversion was found to decrease below that observed for the base catalyst (FeMnO_x) to 50%. Increasing the temperature resulted in significant improvement in the performance of the catalysts, at $90\text{ }^{\circ}\text{C}$ the 12.5% CeO_x catalyst exhibited a conversion of 97%, whereas the

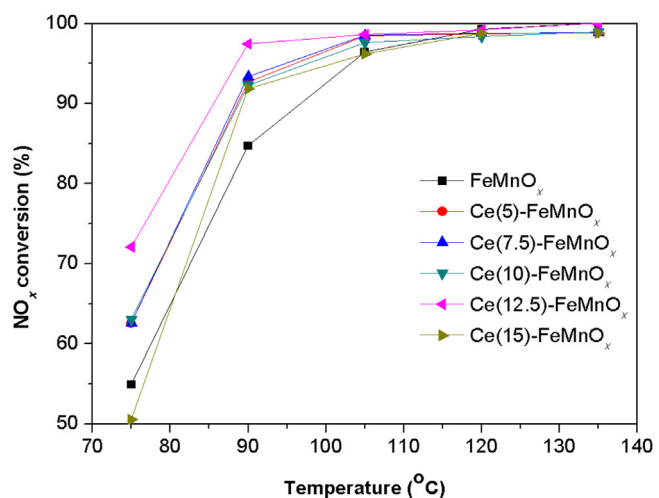


Fig. 1. Low temperature NO_x conversion of FeMnO_x and $\text{Ce}(y)$ catalysts ($y = 5\text{--}15\%$ CeO_x), conditions; $\varphi(\text{NO}) = \varphi(\text{NH}_3) = 0.1\%$, $\varphi(\text{O}_2) = 3\%$, N_2 balance, GHSV = $30,000\text{ h}^{-1}$; reaction temperature = $75\text{--}135\text{ }^{\circ}\text{C}$.

other loading levels resulted in approximately 92% indicating that at higher temperatures CeO_x addition offers significant promotion over FeMnO_x (84%).

3.2. Influence of SO_2 , H_2O and their combination

Operations downstream of the desulphurisation unit leads to inherently low levels of SO_2 in the flue gas however this residual amount would have a negative impact upon the de NO_x activity of the catalysts. Two different methods can be employed to examine the influence of SO_2 upon the activity of these catalysts, isothermal and non-isothermal. The latter of which is not particularly suitable for such a study due to the time scales often involved in achieving a stable catalytic state during low-temperature SCR, hence the former at $120\text{ }^{\circ}\text{C}$ has been employed in this study. After achieving a steady state, 100 ppm SO_2 was added to the simulated flue gas, all of the catalysts exhibited a decrease in NO_x conversion (Fig. 2). The conversion was not found to drop below 90% for any of the catalysts during this study, suggesting that all materials, under the present conditions, exhibit reasonable short term sulphur resistance. However, it showed clearly that all explored catalysts achieve near 100% conversion prior to SO_2 treatment, making a true comparison in terms of activity impossible as all ceria containing catalysts have similar levels of recovery. But FeMnO_x does not significantly recover, indicating a degree of irreversible deactivation occurs over

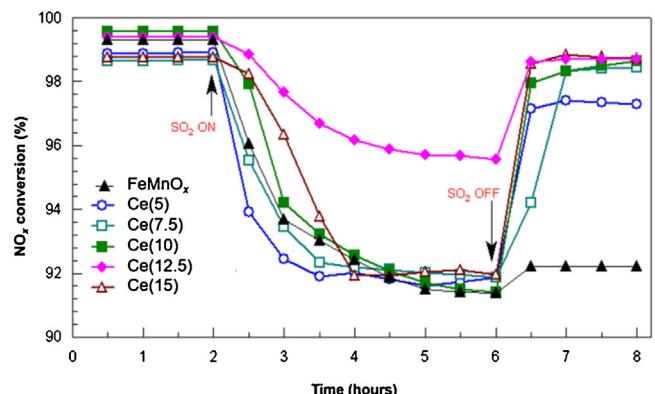


Fig. 2. Influence of SO_2 on NO_x conversion of FeMnO_x and $\text{Ce}(y)$ catalysts ($y = 5\text{--}15\%$ CeO_x), conditions; $\varphi(\text{NO}) = \varphi(\text{NH}_3) = 0.1\%$, $\varphi(\text{SO}_2) = 100\text{ ppm}$, $\varphi(\text{O}_2) = 3\%$, N_2 balance, GHSV = $30,000\text{ h}^{-1}$; reaction temperature = $120\text{ }^{\circ}\text{C}$.

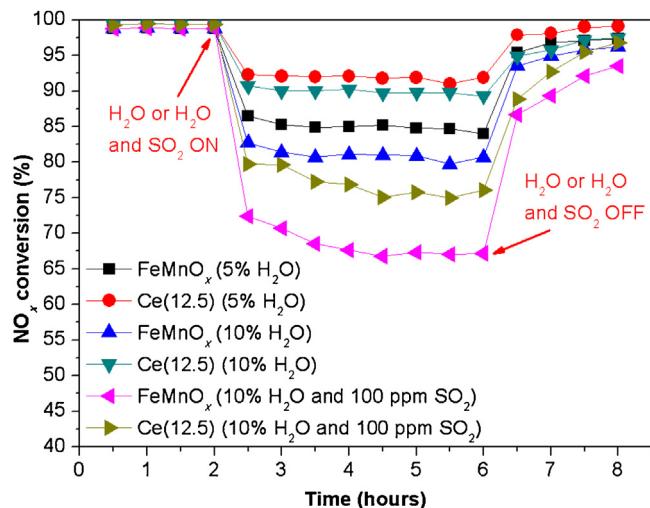


Fig. 3. Influence of H₂O and combined H₂O and SO₂ on NO_x conversion of FeMnO_x and Ce(12.5), conditions; $\varphi(\text{NO})=\varphi(\text{NH}_3)=0.1\%$, $\varphi(\text{H}_2\text{O})=5\%$ or 10% , $\varphi(\text{SO}_2)=100\text{ ppm}$, $\varphi(\text{O}_2)=3\%$, N₂ balance, GHSV = 30,000 h⁻¹; reaction temperature = 120 °C.

this material. On this basis, the influence of H₂O and combined H₂O/SO₂ were explored with FeMnO_x and Ce(12.5), both of which exhibited obvious difference in their conversions in the presence of SO₂ and their abilities to recover after SO₂ removal.

Examination of the H₂O and combined H₂O/SO₂ stability of Ce(12.5) and FeMnO_x were undertaken (Fig. 3). It can be observed that the FeMnO_x catalyst exhibits significantly reduced conversion (85%) upon addition of 5% H₂O to the gas stream, whereas comparatively, the addition of ceria (Ce(12.5)) leads to improved conversion in the presence of H₂O (93%). Both catalysts possess significant recovery characteristics after stopping H₂O, indicating that H₂O does not result in permanent deactivation of either catalyst. Increasing the H₂O concentration to 10% results in a further decline in NO_x conversion for both catalysts, however Ce(12.5) still exhibits superior resilience to the effects of H₂O as indicated by the higher retained conversion (91% vs 81%). In the presence of SO₂ and H₂O, FeMnO_x and Ce(12.5) exhibit much lower conversions than those found for just H₂O or SO₂, both catalysts exhibit a near complete recovery upon stopping the contaminants. This is particularly impressive for FeMnO_x as it exhibits minor recovery in the presence of SO₂ alone, suggesting that water helps to reduce irreversible deactivation caused by SO₂. Zhang et al. examined a TiO₂ supported FeMnO_x catalyst at significantly higher temperature (320 °C). It was found to possess superior H₂O resistance compared to the bulk catalyst utilised in this contribution, but it showed negligible recovery in the presence of SO₂ and the combination of SO₂ and H₂O. The

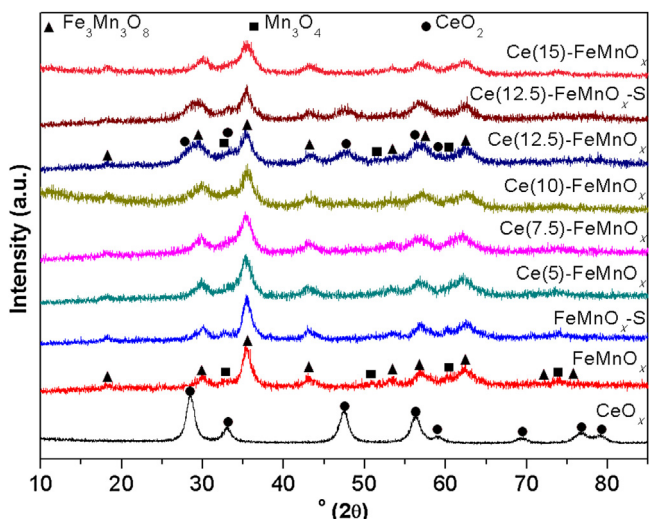


Fig. 4. XRD patterns of as-synthesised CeO_x, FeMnO_x, FeMnO_x-S, Ce(y) catalysts ($y=5\text{--}15\%$ CeO_x) and Ce(12.5)-S.

authors ascribe this deactivation effect to the formation of metal sulphates [29], which seems quite probable, as it is known that (NH₄)₂SO₄ and NH₄HSO₄ start decomposing at 270 °C [30]. However, several differences between the two studies are apparent, the $\text{Fe}_3\text{Mn}_3\text{O}_8$ phase was not observed on the supported catalysts and the temperature employed in the two studies is vastly different. At present the improved recovery in the presence of H₂O and SO₂ cannot be readily explained, further work is currently ongoing with this and a related system in an attempt to rationalise this effect.

3.3. XRD analysis

XRD was used to examine the crystalline phases present in the catalysts (Fig. 4), comparative crystallite sizes were calculated using the Scherrer equation on the reflection ca. $35.0^{\circ} 2\theta$ for $\text{Fe}_3\text{Mn}_3\text{O}_8$ and $28.5^{\circ} 2\theta$ for CeO_2 (Table 1). It was apparent that the CeO_x sample exhibited diffraction peaks (Fig. 4) coinciding with the face centred cubic (fcc) fluorite structure CeO₂ (ICDD PDF card # 65-2975). Its major characteristic diffraction peaks occur at 28.5° , 33.1° , 47.5° and $56.3^{\circ} 2\theta$, which correspond with reflections of the (111), (200), (220) and (311) crystallographic planes respectively. Examination of the FeMnO_x sample indicates the presence of mixed phases, the major contributing crystalline phase could be attributed to the formation of the $\text{Fe}_3\text{Mn}_3\text{O}_8$ phase (ICDD PDF card # 75-0034 = 35.0° , 56.2° and $61.7^{\circ} 2\theta$) and Mn_3O_4 (ICDD PDF card # 89-4837 $2\theta = 32.3^{\circ}$, 36.1° and $59.9^{\circ} 2\theta$). Determination of the Mn₃O₄ phase proved to be quite difficult due to the combi-

Table 1
Surface area, pore volume, pore diameter, crystallite size and specific activity of as-synthesised CeO_x, FeMnO_x, FeMnO_x-S, Ce(y) catalysts ($y=5\text{--}15\%$ CeO_x), Ce(12.5)-S (4 h) and (12 h).

	BET surface area(m ² g ⁻¹)	Pore volume (cm ³ g ⁻¹)	Average pore diameter(nm)	Crystallite size (nm) ^b	Specific activity (nmols ⁻¹ m ⁻²) ^c
CeO _x	62	0.040	4.71	39	–
FeMnO _x	55 ^d (35)	0.090 ^d (0.067)	5.88 ^d (6.37)	33	2.3
Ce(5.0)	68	0.076	5.00	28	2.1
Ce(7.5)	70	0.087	4.98	26	2.1
Ce(10.0)	66	0.072	5.48	26	2.2
Ce(12.5)	59 ^d (52) ^a (34)	0.082 ^d (0.082) ^a (0.073)	5.83 ^d (5.84) ^a (5.85)	25 ^d (23)	2.8
Ce(15.0)	73	0.115	5.47	22	1.8

^a Obtained after 12 h of deNO_x in the presence of 100 ppm SO₂.

^b Calculated from Fig. 3 via the Scherrer equation.

^c Specific activity calculated per unit area (m²), correcting for the use of 2.6 g of catalyst.

^d Data listed in the parentheses were obtained after 4 h of deNO_x in the presence of 100 ppm SO₂.

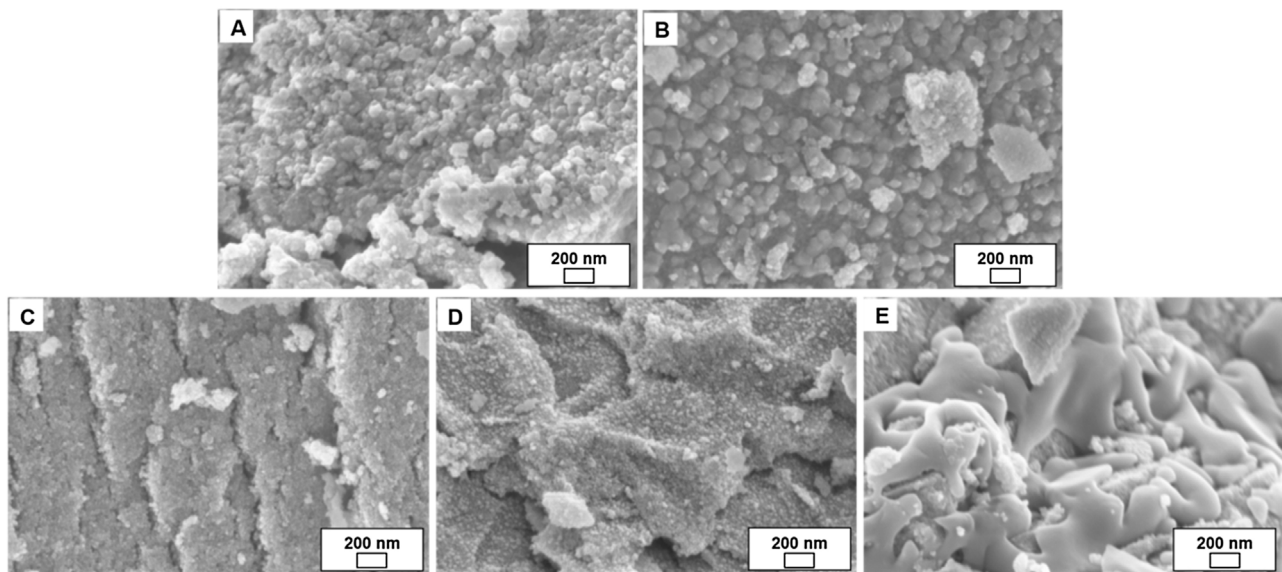


Fig. 5. SEM images of as-synthesised FeMnO_x (A), $\text{FeMnO}_x\text{-S}$ (B), as-synthesised $\text{Ce}(12.5)$ (C), $\text{Ce}(12.5)\text{-S}$ (4 h) (D) and $\text{Ce}(12.5)\text{-S}$ (12 h) (E).

nation of broad, low intensity diffraction peaks, however, a peak was found to exist in a relatively isolated region of the diffraction pattern (approximately $74.5^\circ 2\theta$).

Examination of 5 and 7.5% CeO_x modified catalysts indicates phases related to crystalline CeO_2 were not observed, suggesting that it was present in an amorphous, highly dispersed phase. The isolated peak corresponding to Mn_3O_4 was still present at these loading levels appearing to have broadened, indicating a smaller crystallite size. An increase in CeO_x content (10%) resulted in a material which exhibited crystalline CeO_2 , as evidenced by the appearance of a low intensity diffraction peak at $47.5^\circ 2\theta$. The XRD pattern of $\text{Ce}(12.5)$ demonstrated that larger ceria crystallites were present on the catalyst, in addition to the apparent loss of the crystalline Mn_3O_4 phase. The major CeO_2 diffraction peak had shifted to higher diffraction angle compared to the standard ceria sample ($47.5^\circ 2\theta$) suggesting incorporation of a smaller metal ion into the ceria lattice [31,32]. It was found that $\text{Ce}(15)$ exhibited no ceria diffraction peaks, in conjunction with the reappearance of the crystalline Mn_3O_4 phase. Increased amounts of CeO_x , resulted in a general reduction of the $\text{Fe}_3\text{Mn}_3\text{O}_8$ crystallite size, which is similar to the results obtained by Huang et al. for $\text{V}_2\text{O}_5\text{-CeO}_2/\text{TiO}_2$ [28]. Based upon previous observations of the active phase in FeMnO_x , it is suggested that the enhancement in conversion may arise due to the formation of a secondary or new active phase which is attributed to a CeO_x solid solution. Examination of both FeMnO_x and $\text{Ce}(12.5)$ after deNO_x in the presence of SO₂, indicates no obvious change in their diffraction patterns, suggesting that no crystalline sulphate phases were formed.

3.4. BET, BJH and SEM analysis

N_2 adsorption was utilised to determine the surface area, pore-based characteristics and specific activity in relation to surface area of the catalysts. All catalysts containing ceria exhibited higher surface area than the standard bimetallic oxide catalyst (Table 1), however, no obvious trend was found relating increased amounts of CeO_x incorporation to surface area, pore volume or average pore diameter. It was found that the most active catalyst at 75°C ($\text{Ce}(12.5)$) possessed the second lowest surface area and crystallite size, while $\text{Ce}(15)$ had the highest surface area, smallest crystallite size and specific activity. These results indicate that enhanced

low temperature activity is not attributable to the generation of an increased number of active sites via surface area enhancement and that a complex interplay exists between properties such as, crystal phases, amorphous phases, localised surface structure and composition.

After 4 h treatment with 100 ppm SO₂, catalysts were characterised to examine any alterations to the textural properties due to the deactivation phenomena observed in Fig. 2. It was found that both FeMnO_x and $\text{Ce}(12.5)$ exhibit surface area losses during SO₂ treatment (Table 1). It has been demonstrated that FeMnO_x exhibits an unrecoverable loss in conversion and also a significant reduction in surface area ($55\text{--}35 \text{ m}^2 \text{ g}^{-1}$), which is associated with pore blockage, as indicated by the decrease in pore volume and increase in the average pore diameter. SEM of FeMnO_x prior to and after exposure to SO₂ (Fig. 5A and B respectively), indicates a minor degree of aggregation at the surface, however little can be ascertained regarding the change in pore structure from this technique due to the relatively small size of the pores. $\text{Ce}(12.5)$ exhibits a lower surface area loss ($59\text{--}52 \text{ m}^2 \text{ g}^{-1}$), in conjunction with no obvious change in the pore structure. (Table 1). On the basis of SEM imaging it can be observed that the as-synthesised catalyst (Fig. 5C) exhibited quite a high degree of surface defects on the bulk particle, after exposure to SO₂ for 4 h (Fig. 5D) there were fewer observed. After 12 h (Fig. 5E) the surface had changed drastically, becoming relatively defect-free, which coincided with a significant decrease in surface area ($33 \text{ m}^2 \text{ g}^{-1}$) and pore volume (Table 1).

Supported vanadia catalysts are highly susceptible to the formation of NH_4HSO_4 , which is known to deposit readily on the surface of the catalyst, blocking the pores [30,33]. Recently Kwon et al. compared vanadia supported on $\text{Ti}_{1-x}\text{Ce}_x\text{O}_{2-s}$ with TiO_2 in SO₂ contaminated SCR, they demonstrated that the presence of Ce species led to an improvement in SO₂ resistance of the catalyst. It was suggested that the formation of $\text{Ce}_2(\text{SO}_4)_3$ led to significant consumption of SO₂, which inhibited the formation of NH_4HSO_4 , resulting in a longer lifetime [30]. Mn and Fe-based catalysts are also known to be susceptible to the formation of NH_4HSO_4 and stable metal sulphates, which significantly decreases the reducibility of the metal ion species [34]. FeMnO_x may deactivate via pore plugging due to NH_4HSO_4 , however the formation of metal sulphate/sulphite cannot be ruled out. The modified catalyst is found to be more susceptible to surface modification, possibly via the for-

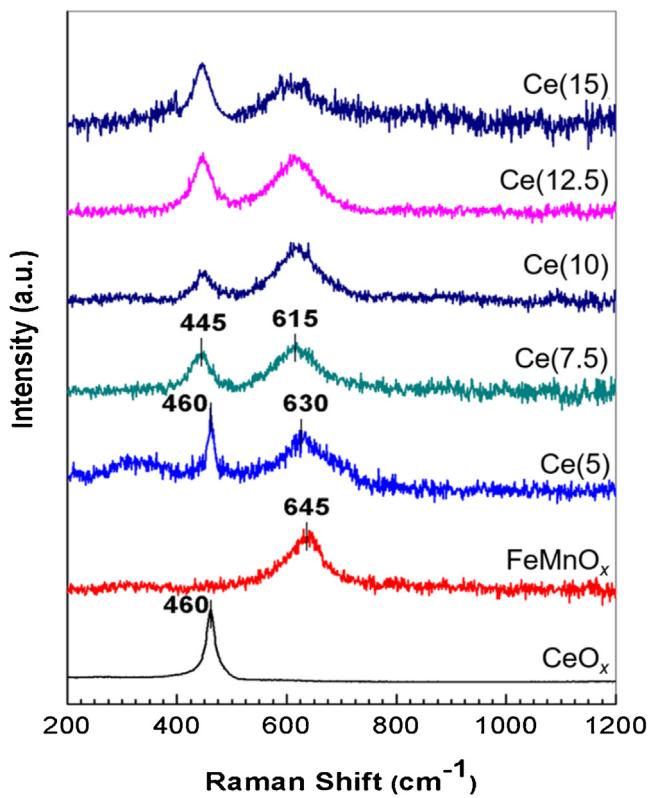


Fig. 6. Raman spectra of as-synthesised CeO_x, FeMnO_x and Ce(y) catalysts (y = 5–15% CeO_x).

mation of metal sulphates during exposure to SO₂, no obvious loss in pore volume was observed over the initial four hour reaction period suggesting that NH₄HSO₄ formation was suppressed.

3.5. Raman analysis

Raman spectroscopy (Fig. 6), is a suitable technique to examine variations in vibrational modes associated with CeO₂ and FeMnO_x as ceria content increased. Cubic CeO₂ displays an intense band at approximately 460 cm⁻¹, which is consistent with previous publications [35,36] and is assigned to the symmetric breathing mode of O atoms around Ce⁴⁺ [37,38]. Fe(0.4)-MnO_x exhibits a single signal corresponding to Fe₃Mn₃O₈ and Mn₃O₄ at 645 cm⁻¹, which is attributed to the vibration of Mn-O [21,39]. No evidence of amorphous Fe₂O₃ or Fe₃O₄ was found in the wavenumber range 200–400 cm⁻¹, suggesting that Fe species had been fully incorporated into the Fe₃Mn₃O₈ structure [40,41]. Addition of ceria (5%), resulted in no obvious shift or broadening in the signal ca. 460 cm⁻¹, however, the Mn-O vibrational mode was shifted to 630 cm⁻¹. As the amount of ceria increased to 7.5% both bands shifted to lower wavenumbers (445 cm⁻¹ and 615 cm⁻¹ respectively), beyond this level no further change in either peak position was observed. Broadening of the band associated with CeO₂ indicates that either metal ions were incorporated into the lattice [39] or ceria crystallites were reduced in size [20]. The appearance of broad diffraction peaks for Ce(10) and Ce(12.5) (Fig. 4) with no narrowing of the Raman band negates the latter argument. The apparent red shift of the signal position is attributed to lattice contraction [32], due to the incorporation of smaller metal ions (Mn and/or Fe) into the ceria lattice. Venkataswamy et al. demonstrated that the formation of Fe/Mn doped ceria resulted in a new band arising at 594–597 cm⁻¹, which was attributed to oxygen vacancies within the ceria lattice [39]. They suggested that a band at 644 cm⁻¹ for Mn-doped ceria

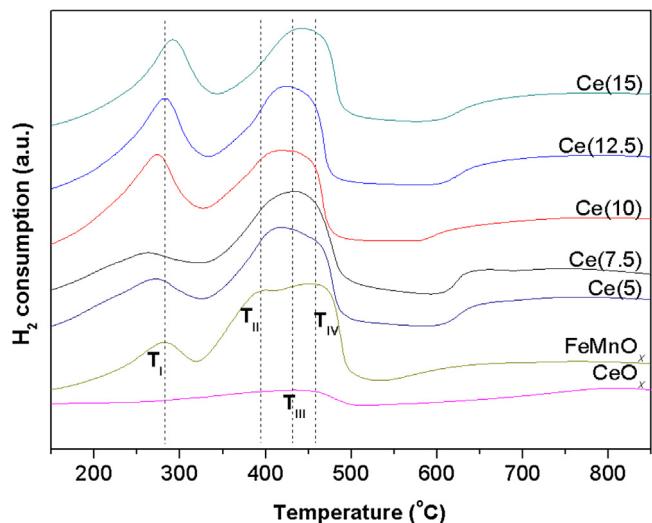
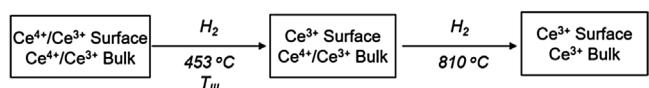


Fig. 7. TPR profiles of as-synthesised CeO_x, FeMnO_x and Ce(y) catalysts (y = 5–15% CeO_x).

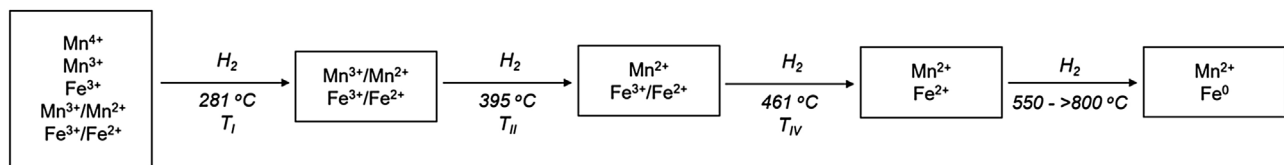
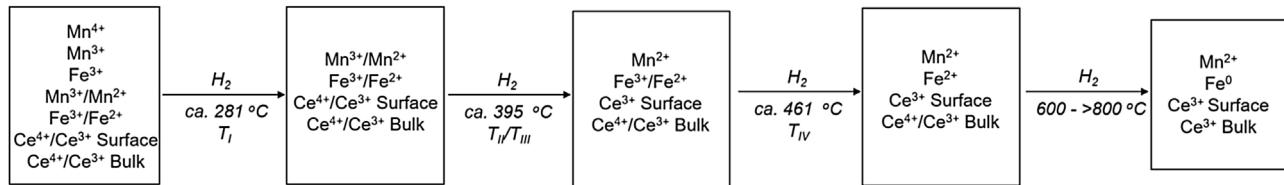
was also associated with oxygen vacancies, however this is most likely associated with amorphous MnO_x species present on the surface of the catalyst. Given the relatively low concentration of ceria, moderate signal to noise ratio, broad bands and the occurrence of the Mn-O vibration mode, the signal assigned to oxygen vacancies was not observed in this study. The red shift in the band ca. 645 cm⁻¹ may be associated with reduction of the Fe₃Mn₃O₈ crystallite size. Care must be taken making this suggestion due to the influence other factors upon band position, broadness and intensity [20]. Raman spectroscopy verifies the formation of a solid solution, which agrees well with XRD, however, questions still remain regarding its influence upon activity. In an attempt to probe changes in activity and sulphur resistance, bulk properties, such as reducibility (a critical parameter for redox catalysis) must be examined.

3.6. TPR analysis

TPR profiles are presented in Fig. 7 for all catalysts and CeO_x, it can be observed that the latter generates two peaks ca. 453 (denoted as T_{III} in Fig. 7) and 810 °C, which can be assigned to the reduction of surface and bulk Ce⁴⁺ respectively (summarised in Scheme 1) [31,32]. Based upon our previous work, MnO_x exhibits two reduction events, a small feature ca. 187 °C and a much broader asymmetric feature at around 439 °C [42]. A similar TPR profile was observed by Yang et al. who suggested that this represented the reduction of Mn₃O₄ via two steps. The first step was said to be associated with the reduction of a weaker Mn-O bond, which yielded a more recalcitrant structure, resulting in further reduction at higher temperature [43]. However sufficient evidence was not provided to support the claim of this new intermediate MnO_x structure. Several authors have provided a different explanation, suggesting that amorphous Mn₂O₃ initially reduces to Mn₃O₄ before converting to MnO at higher temperature [42,44], this is the more likely of the two proposals and hence will be considered as the reductive process for MnO_x. FeO_x is found to exhibit three major reduction features at 362, 638 and above 700 °C, which are associated with the reduc-



Scheme 1. Reduction stages of CeO_x.

Scheme 2. Reduction stages of FeMnO_x .Scheme 3. Reduction stages of $\text{Ce}(y)$ catalysts ($y = 5\text{--}15\%$ CeO_x).

tion of Fe_2O_3 to Fe_3O_4 , Fe_3O_4 to FeO and FeO to Fe^0 [42]. FeMnO_x has a more complex TPR profile with three very broad reduction features, the first is observed starting below 150°C and maximises at approximately 281°C . The second is a highly asymmetric feature which intersects the initial reduction and is observed between 325 and 525°C , based upon the shape of the peak, it seems that at least two reductive transitions occur in this region (these features are denoted as T_1 , T_{II} and T_{IV} respectively, in Fig. 7). The final feature begins at 550°C and continues beyond 800°C . On the basis of XRD data it can be determined that the major crystalline phases may be attributed to $\text{Fe}_3\text{Mn}_3\text{O}_8$ and Mn_3O_4 . Work undertaken by Chen et al. demonstrates that a physical mixture of MnO_x and FeO_x results in a lowering of the reduction temperature for the Fe_3O_4 to FeO and FeO to Fe^0 transitions, however little change was observed for the Fe_2O_3 to Fe_3O_4 reduction. It must be noted that the lower temperature reduction observed for MnO_x was shifted to significantly higher temperature in conjunction with a minor temperature decrease in the Mn_3O_4 to MnO transition [42]. With these previous observations in mind the reductions observed for FeMnO_x can be assigned as follows, the initial feature (*ca.* 281°C) is attributed to the transformation of high oxidation state ions, namely those associated with $\text{Mn}^{4+}/\text{Mn}^{3+}$ and perceptibly Fe^{3+} in easily reducible sites. The broad feature between 325 and 525°C is associated with numerous different reductive transitions, in the lower temperature region reductions associated with Mn^{3+} in $\text{Fe}_3\text{Mn}_3\text{O}_8$ and Mn_3O_4 phases, the higher temperature region of this feature is attributed to the transition of Fe^{3+} in $\text{Fe}_3\text{Mn}_3\text{O}_8$ to Fe^{2+} . The final feature is assigned to the reduction of Fe^{2+} to Fe^0 (summarised in Scheme 2).

The addition of ceria results in significant improvement of low temperature reducibility (Fig. 7), the feature (T_1) is found to broaden significantly, with maximised hydrogen consumption achieved at lower temperature, which is optimised at 7.5 mol% ceria. Further addition of ceria results in a significant enhancement in the intensity of this feature suggesting that, more, higher oxidation state species are reduced at lower temperature. It is rather obvious that the broad feature observed for FeMnO_x changes drastically as ceria content increased, indicating that reducibility of the catalyst improves. Based upon the assigned reductions in this range (Scheme 2) it can be observed that the transitions associated with the spinel-type structures occur in this region. As mentioned previously the lower temperature range (T_{II}) is assigned to the reduction of Mn^{3+} species in $\text{Fe}_3\text{Mn}_3\text{O}_8$ and Mn_3O_4 and at higher temperature (T_{IV}) the Fe species in $\text{Fe}_3\text{Mn}_3\text{O}_8$. It is apparent that the shift in the feature is towards higher temperature (T_{IV}), suggesting that there is a decline in the lower temperature contribution (T_{II}) with ceria addition. On this basis it may be suggested that Mn-species are preferentially incorporated into the ceria lattice in comparison

Table 2
 NH_3 -, NO - and SO_2 -TPD peak areas for CeO_x , FeMnO_x and $\text{Ce}(y)$ catalysts ($y = 5\text{--}15\%$).

Catalyst	Total desorption peak area (mVs^{-1})		
	NH_3 -TPD	NO -TPD	SO_2 -TPD
CeO_x	1006	2696	–
FeMnO_x	22092	23510	18593
$\text{Ce}(5)$	11986	12251	14940
$\text{Ce}(7.5)$	11967	11076	11643
$\text{Ce}(10)$	5417	12345	11375
$\text{Ce}(12.5)$	5158	8102	5660
$\text{Ce}(15)$	10329	7877	6055

to Fe-species. This would certainly match the apparent increase in reducibility (T_1) and aligns well with observations made by Ramana et al., who demonstrate that $\text{Ce}_{1-x}\text{Mn}_x\text{O}_{2-\sigma}$ catalysts exhibit significantly enhanced T_1 reduction peaks and smaller mid-temperature peaks (T_{II}) [32]. It was found that the incorporation of Fe into ceria resulted in an enhancement effect in the mid temperature region (comparable to T_{II}) [32], however this is not exhibited by the data within this contribution. It must be noted that both Ramana et al. and Venkataswamy et al. found no separate reduction feature attributed to surface Ce^{4+} , suggesting that this must occur within the same range as that observed for both the Fe and Mn reductions [32,39]. It can be determined that the reducibility of surface Ce^{4+} is enhanced and occurs in the mid-temperature range (T_{II}). Bulk Ce^{4+} was found to reduce in a similar region to that observed for ceria by Ramana et al., a notable feature is present at temperatures above 600°C in Fig. 7, which may be associated with both Fe^{2+} to Fe^0 and bulk Ce^{4+} to Ce^{3+} reductive transitions (summarised in Scheme 3) [32].

3.7. NH_3 -, NO - and SO_2 -TPD

To gain further insight into these complex structure-activity relationships, a series of TPD experiments were conducted to compare desorption characteristics of chemisorbed NH_3 (Fig. 8A), for the purposes of comparison the total desorption area was tabulated for each catalyst (Table 2). It can be observed in Fig. 8A that CeO_x exhibits a very broad low intensity desorption profile. Hence, it is apparent that CeO_x exhibits a relatively low number of acid sites possessing a large variance in strength, which is in very good agreement with results obtained by Shen et al. [45]. FeMnO_x exhibits a profile indicative of a large number of total acid sites, in the weak acid strength region one very small desorption peak can be observed centring around 210°C , at higher temperatures a very broad desorption trace is observed from approximately $300\text{--}850^\circ\text{C}$. The latter appears to exhibit four potential features *ca.* 500, 550, 700

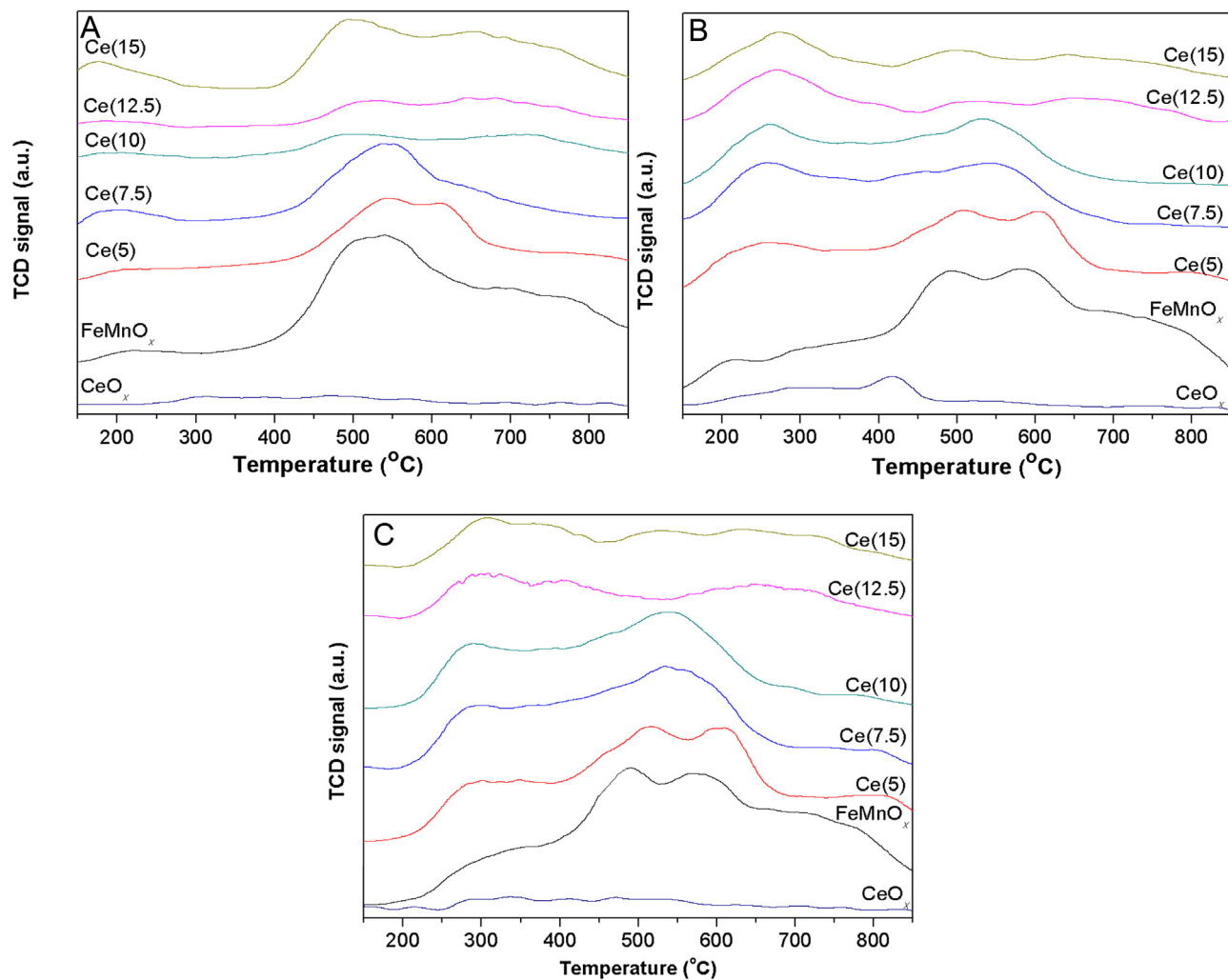


Fig. 8. NH₃- (A), NO— (B) and SO₂-TPD (C) of as-synthesised CeO_x, FeMnO_x and Ce(y) catalysts (y = 5–15% CeO_x).

and 775 °C, which coincides with the removal of strongly bound ammonia on acid sites, this clearly indicates the presence of a significant spectrum of acid site strengths and, by association, a large number of differing acid site species and/or environments. Upon addition of CeO_x (5%) a large reduction in overall signal intensity (Table 2) was observed, indicating a significant loss of acidic character. Fig. 8A shows that a general reduction in all acid sites occurs, however a significant decline in the feature at 500 °C and the appearance of a reductive transition at 625 °C. An increase in CeO_x loading to 7.5% resulted in minor reduction of the peak area (Table 2), however a significant change in Fig. 8A was apparent indicating a noticeable decrease in intensity of the peak at 625 °C and an increase in the lower temperature peaks ca. 210 and 550 °C. Ce(10) and Ce(12.5) result in significantly reduced desorption profiles, suggesting a significant loss in the number of acid sites on the catalyst. Upon increasing the loading to 15% the amount of desorbed NH₃ increased significantly (Table 2). This increase in NH₃ desorption coincides with the re-emergence of crystalline Mn₃O₄, which was not observed to any degree at 10 and 12.5% ceria addition. Deorsola et al. found that MnO_x catalysts which contained crystalline Mn₃O₄ exhibited significantly enhanced NH₃-TPD patterns, suggesting that this phase enhances the acidity of the catalysts [46]. These results tentatively suggest that low levels of ammonia adsorption is a key characteristic of catalysts exhibiting higher low-temperature SCR activity, but, this parallels findings made in

TPR studies in that catalysts containing both 10 and 12.5% CeO_x appear to exhibit this optimised characteristic.

It has been suggested previously that the most important facet of low-temperature SCR is the initial oxidation of NO to NO₂ [20]. This was later challenged by Salazar et al. who suggested, via the utilisation of active component separation, that the initial process generates a more labile species, such as HNO₂ [47]. Regardless of the exact species, it is agreed by both that NO oxidation is an important mechanistic step in the SCR process. An examination of the NO-TPD properties of all catalysts was undertaken (Fig. 8B), it can be observed that CeO_x exhibits a broad desorption feature from approximately 175–600 °C with several maxima ca. 275 °C (nitrosyl species) and 425 °C (metal nitrate) [48]. However, the overall signal intensity was low in comparison to the other catalysts (Table 2). FeMnO_x generates a significant desorption profile (Fig. 8B) exhibiting three features (210, 490 and 590 °C), suggesting a number of NO_{ads} species are present in different chemical environments. The addition of ceria exhibits a pronounced effect upon this profile, indicating an increase in the contribution from lower temperature desorption. Conversely the two higher temperature features initially reduce in intensity upon addition of 5% CeO_x and above this loading a single feature which gradually shifts towards lower temperature is formed. Similar observations were made by Lee et al. where it was found that the addition of ceria to Sb-V₂O₅/TiO₂ led to significant improvement in low temperature desorption char-

acteristics of their catalysts [49]. However some differences are apparent, the aforementioned study exhibits an increase in total acidity upon addition of ceria, whereas these systems are bulk catalysts with a support based additive. It is suggested that the results in this study occur due to ceria interacting with the particles, effectively blocking large portions of the active surface, while simultaneously improving its activity. Doping of Mn^{x+} and Fe^{x+} into ceria and surface modification of accessible $Fe_3Mn_3O_8$ via geometric and/or electronic interactions commonly observed in Ce/Cu based systems are expected to play a key role in this enhancement effect [31,32,50]. Hence, it can be determined that the desorption features which appear to be beneficial for enhanced low temperature activity are those that exhibit relatively low levels of NH_3 desorption at moderate temperature and which exhibit significant low temperature NO desorption, with minimal moderate and high temperature contributions.

Examination of the SO_2 -TPD profile (Fig. 8C) for ceria reveals only a very small desorption contribution observed across the range, which maximises between 200 and 600 °C. It has been reported that ceria is able to inhibit the formation of NH_4HSO_4

Table 3
Surface atomic concentration of $FeMnO_x$, $FeMnO_x$ -S, $Ce(y)$ ($y = 5, 10$ and 12.5%) and $Ce(12.5)$ -S.

Catalyst	Surface concentration (atm.%)				
	Ce	Fe	Mn	O	$Fe/(Fe + Mn)$
$FeMnO_x$	—	10.83	22.27	66.90	0.33
$FeMnO_x$ -S	—	7.92	22.34	69.74	0.26
$Ce(5)$	0.38	7.51	18.09	74.02	0.29
$Ce(10)$	0.56	7.04	17.01	75.40	0.29
$Ce(12.5)$	0.68	8.23	19.37	71.72	0.30
$Ce(12.5)$ -S	0.48	7.62	18.29	73.61	0.29

during reaction [51]. It has also been demonstrated that ceria containing Mn or Fe catalytic systems efficiently utilise SO_2 to generate additional acidic properties, while effectively protecting metal ions associated with NO adsorption (Fe and/or Mn) [52,53]. $FeMnO_x$ exhibits the most intense TPD profile, with several desorption events observed at 350, 490, 575, 725 and 775 °C. The feature observed at 350 °C, is attributed to the removal of SO_2 species adsorbed on weakly acidic centres as suggested by Kijlstra et al.

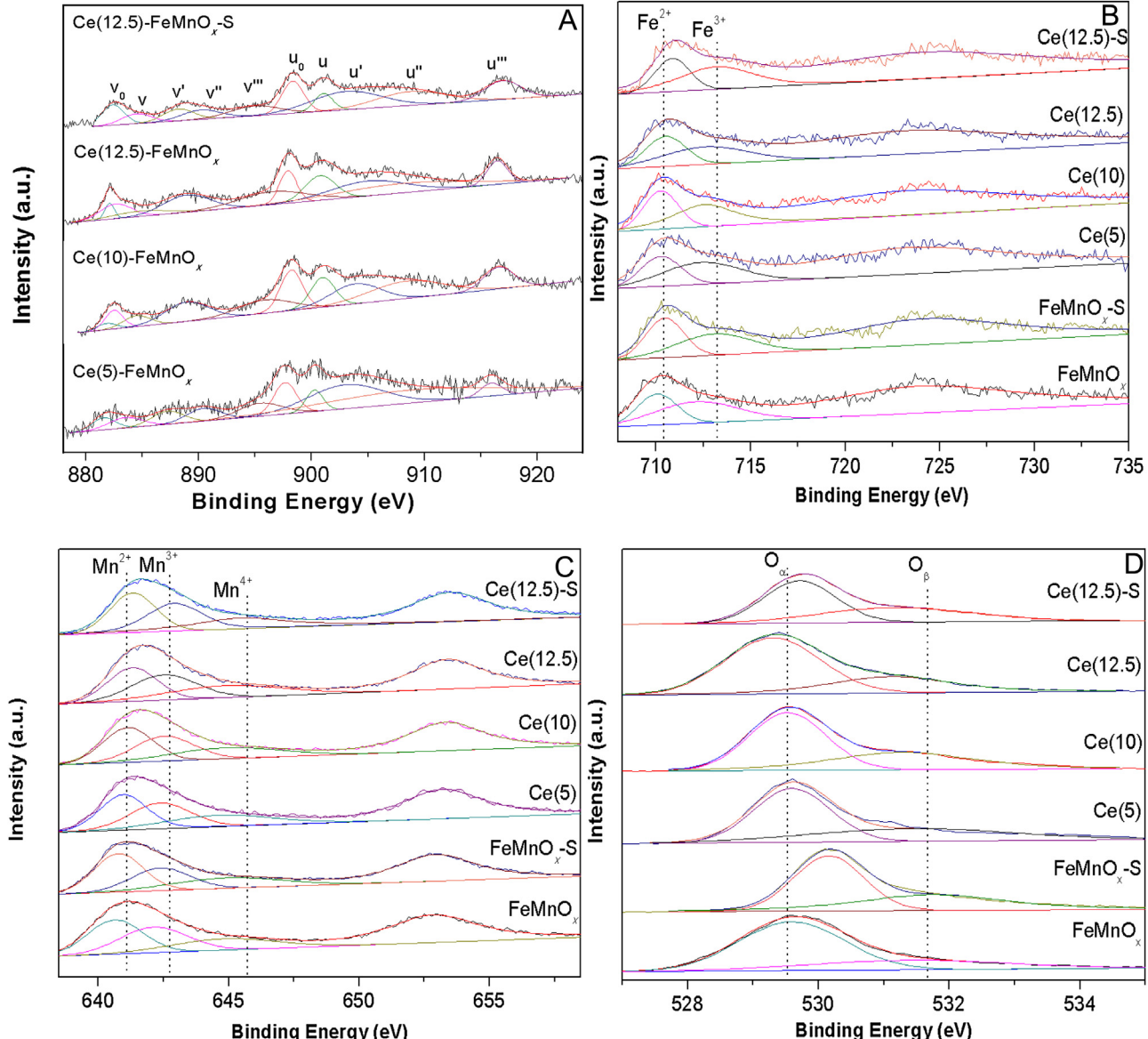


Fig. 9. XPS analysis of Ce (A), Fe (B), Mn (C) and O (D) for as-synthesised $FeMnO_x$, $Ce(y)$ ($y = 5, 10$ and 12.5%) and $Ce(12.5)$ -S.

[54]. It was found by Siriwardane et al. that thermal decomposition of both FeSO_4 and $\text{Fe}_2(\text{SO}_4)_3$ occurred across the same temperature range (500–600 °C) [55], however they exhibited different profiles. FeSO_4 generated a more intense mass loss initially, whereas more mass loss was found at higher temperatures for $\text{Fe}_2(\text{SO}_4)_3$. Hence it is suggested that the observed TPD features at 490 and 575 °C are associated with decomposition of Fe^{2+} and Fe^{3+} sulphate species respectively. Higher temperature features are found to be in the range expected for decomposition of manganese sulphate, Wu et al. demonstrated that MnSO_4 decomposed between 750 and 900 °C [56]. It is tentatively suggested that due to the different Mn^{2+} sites present in the catalyst, namely those associated with $\text{Fe}_3\text{Mn}_3\text{O}_8$ and Mn_3O_4 , that the two features ca. 725 and 775 °C are attributable to the decomposition of sulphate species in different chemical environments. Increased ceria content results in an overall reduction in SO_2 desorption, which maximises at 12.5% addition (Table 3). Similarly a comparison of TPD profiles demonstrates that ceria promotes lower temperature desorption with a simultaneous reduction in higher temperature contributions, this effect is most apparent for Ce(12.5) and Ce(15).

Hence, these results demonstrate that ceria addition significantly alters the bulk properties of the catalysts, specifically those associated with adsorption/desorption, which are key parameters for catalytic activity. The addition of ceria results in a significant decrease in the number of available adsorption sites, it is apparent that the remaining redox sites become more active suggesting a synergistic interaction exists at 12.5% that is not completely apparent at higher or lower loadings.

3.8. XPS analysis

Comparative investigations were undertaken to determine the surface chemical states of Ce, Fe, Mn, and O species for FeMnO_x , $\text{FeMnO}_x\text{-S}$, Ce(y) ($y=5, 10$ and 12.5% ceria) and Ce(12.5)-S catalysts (Fig. 9). It can be observed in Fig. 9A that two major regions are observed in Ce spectra, 882–896 eV and 898–917 eV, coinciding with $\text{Ce } 3d_{5/2}$ and $\text{Ce } 3d_{3/2}$ respectively. These regions and the resulting signals are in agreement with values observed in works related to ceria based solid solutions [32]. Two common peak fitting models exist for deconvolution of the Ce signals, the first utilises an 8 peak fitting pattern, in this instance only 2 peaks are considered for their contribution to the total Ce^{3+} , however this can lead to underestimation of the real values, while arguably retaining the effective trend [57]. The more reliable model utilises 10 individual peak assignments; v_0, v, v', v'' and v''' , which are associated with deconvoluted signals in the $\text{Ce } 3d_{5/2}$ region and u_0, u, u', u'' and u''' in the $\text{Ce } 3d_{3/2}$ region, four of these (v_0/u_0 and v'/u') are ascribed to Ce^{3+} and 6 ($v/u, v''/u''$ and v'''/u''') to Ce^{4+} [32]. Fig. 9B illustrates the

spectra obtained for Fe, two distinguishable signals are observed $\text{Fe } 2p_{3/2}$ (710.0–711.0 eV) and $\text{Fe } 2p_{1/2}$ (723.5–724.5 eV). Peak fitting deconvolution of the $\text{Fe } 3d_{3/2}$ peak indicates the presence of two different Fe species, Fe^{2+} (710.0–710.6 eV) and Fe^{3+} (712.4–712.7 eV). The same deconvolution procedure was applied for the $\text{Mn } 3p_{3/2}$ signal in Fig. 9C, it can be reliably separated into three contributing signals 640.5–641.1 eV, 642.2–643.0 eV and 645.5–646.8 eV. The position of samples not treated with SO_2 are similar to those observed for $\text{Mn } 3p_{3/2}$ in CrMnO_x systems [20], hence these signals can be assigned to Mn^{2+} , Mn^{3+} and Mn^{4+} respectively. It has been shown previously that treatment of catalysts with SO_2 results in increased binding energy of transition metal ions [58], which may occur outside of the normally anticipated eV range.

Table 3 displays the determined surface concentration (atm.%) of the catalysts. FeMnO_x exhibits a surface enrichment of Fe (0.33) as determined from $\text{Fe}/(\text{Fe} + \text{Mn})$, however the ceria modified samples have effectively the same ratio of 0.29–0.30, which is lower than the theoretical bulk composition (0.4). The highest surface concentration of metals was found for FeMnO_x , the addition of ceria in all instances resulted in a significant decline of the surface quantities of both Fe and Mn, however, of the modified variants Ce(12.5) exhibits maximised surface Fe and Mn concentrations. It can be observed in Fig. 9D and Fig. S1 that asymmetric peaks were observed in the O 1 s spectra of all samples, deconvolution of these signals leads to two distinctly different peaks, 529.3–529.9 eV, which is assigned to lattice oxygen (O^{2-}) and 531.1–531.5 eV, which can be attributed to several forms of oxygen species such as, chemisorbed O_2^{2-} or O^- species [31,32].

Table 4 displays calculated concentrations of Fe, Mn and O species. It has been suggested previously that surface chemisorbed oxygen species play a significant role in oxidation reactions [5]. NO oxidation is suggested to play a crucial role in low-temperature SCR [20], hence it may be expected that the most active catalyst possess the largest amount of active oxygen species [42,59], however, this is not the case (Table 4). The most active catalyst, has less chemisorbed oxygen at its surface than a number of the other catalyst, but it also has the lowest O 1s binding energy, indicating improved oxygen mobility. NO oxidation is known to be the rate limiting step if the fast SCR reaction proceeds via the L-H mechanism, however for the E-R mechanism NO_2 desorption dominates the reaction kinetics. On related mixed metal oxide catalysts NO oxidation has been suggested to proceed via the L-H mechanism, hence, chemisorbed surface oxygen and NO adsorption are key parameters for enhanced activity [20,42]. To try and elucidate the major factor affecting the activity of these catalysts the obtained conversions for FeMnO_x and Ce(y) (where $y=5\text{--}15$ mol% ceria addition) were plotted against the ratio between their total NO desorption area (mV s^{-1}) and surface O (atm.%) (Fig. 10A),

Table 4

Binding Energies (eV) and surface speciation of FeMnO_x , $\text{FeMnO}_x\text{-S}$, Ce(y) ($y=5, 10$ and 12.5%) and Ce(12.5)-S.

Catalyst	Surface concentration (atm.%)						
	$\text{Fe } 2p_{3/2}$ (eV)		$\text{Mn } 2p_{3/2}$ (eV)			$\text{O } 1s$ (eV)	
	Fe^{2+}	Fe^{3+}	Mn^{2+}	Mn^{3+}	Mn^{4+}	$\text{O}^{2-} (\text{O}_\alpha)$	$\text{O}^-/\text{O}_2^{2-} (\text{O}_\beta)$
FeMnO_x	710.0	712.0	640.6	642.1	644.8	529.6	531.5
	4.40	6.43	8.55	8.02	5.70	48.70	18.20
$\text{FeMnO}_x\text{-S}$	710.7	7133	640.5	642.6	645.0	530.1	531.9
	3.80	4.12	9.76	6.75	583	39.12	30.62
Ce(5)	710.2	712.4	641.2	642.6	644.9	529.6	531.5
	3.08	4.43	6.98	6.33	4.78	45.15	28.87
Ce(10)	710.3	7125	641.1	642.5	644.9	529.5	531.3
	3.04	4.00	6.72	5.68	4.61	46.75	28.65
Ce(12.5)	710.5	712.6	641.3	642.5	644.9	529.3	531.3
	3.68	4.55	6.88	678	5.71	49.06	22.66
Ce(12.5)-S	710.6	712.7	641.3	642.5	645.2	529.9	531.5
	3.71	3.91	6.66	6.45	5.18	42.47	31.14

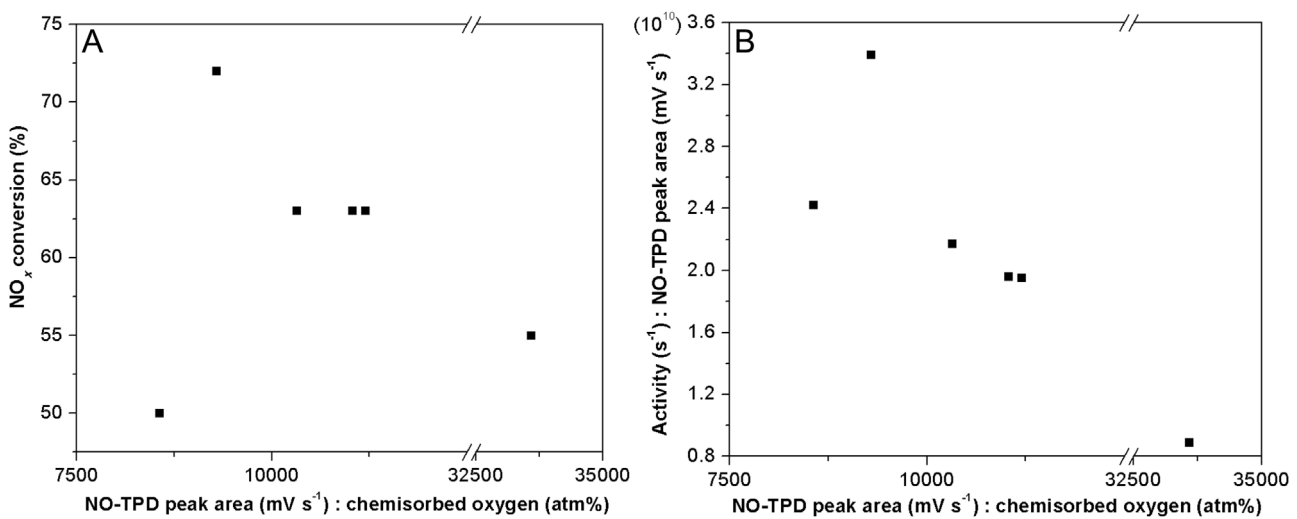


Fig. 10. NO_x conversion (%) against NO-TPD peak area (mV s⁻¹): chemisorbed oxygen (atm%) (A), Activity (s⁻¹): NO-TPD peak area (mV s⁻¹) against NO-TPD peak area (mV s⁻¹): chemisorbed oxygen (atm%) (B). (NO-TPD peak area refers to values corrected against the mass of catalyst used in reaction (2.6 g) compared to TPD (100 mg), which are representative of total NO adsorption sites and chemisorbed surface oxygen O_B, determined via XPS).

which is representative of the ratio between the NO adsorption sites and chemisorbed surface oxygen. Little can be ascertained from this data, except for the fact that there appears to be a trend similar to a volcano plot, however it is not possible to discern the differences between catalysts containing 5–10 mol% ceria. To further explore this trend, the conversions were converted to activity values (s⁻¹) and corrected against the NO-TPD peak area, giving final values comparable to turnover numbers. Plotting these values against the NO adsorption sites to chemisorbed surface oxygen ratio (Fig. 10B) a more convincing volcano plot is established, which demonstrates that all catalysts containing ceria exhibit enhancements in turnover, which are between 2 and 4 times greater than FeMnO_x at 75 °C. This indicates a clear effect on the catalytic activity which appears to be attributable to the fast-SCR reaction. The standard SCR reaction is known to be heavily reliant upon NH₃ adsorption sites, which when increased gives rise to higher conversion [60–62]. However in these systems a notable decrease is found in the number of NH₃ adsorption sites, in conjunction with an increase in conversion, suggesting that standard SCR plays a minor role compared to fast-SCR. Hence, ceria appears to tune the catalytic surface by adjusting the ratio between NO adsorption sites

Table 5

Surface atomic concentration of Ce³⁺ and Ce⁴⁺ of Ce(y) (y=5, 10 and 12.5%) and Ce(12.5)-S.

Catalyst	Surface ratio		Surface concentration (atm.%)		
	Ce ³⁺ / (Ce ³⁺ + Ce ⁴⁺)	Ce ⁴⁺ / (Ce ³⁺ + Ce ⁴⁺)	Ce	Ce ³⁺	Ce ⁴⁺
Ce(5)	0.44	0.56	0.38	0.17	0.21
Ce(10)	0.36	0.64	0.56	0.20	0.36
Ce(12.5)	0.32	0.68	0.68	0.22	0.46
Ce(12.5)-S	0.47	0.53	0.48	0.23	0.25

and chemisorbed surface oxygen, which when optimised gives a significant enhancement in the activity of the catalyst.

Examination of the SO₂ treated catalysts shows that FeMnO_x and Ce(12.5)-S exhibit significantly different surface compositions and increased binding energies of all observed species as a result of SO₂ exposure (Tables 4 and 5). It was found over FeMnO_x that very little change occurred in the total surface Mn concentration, however it was noted that there was an apparent increase in the

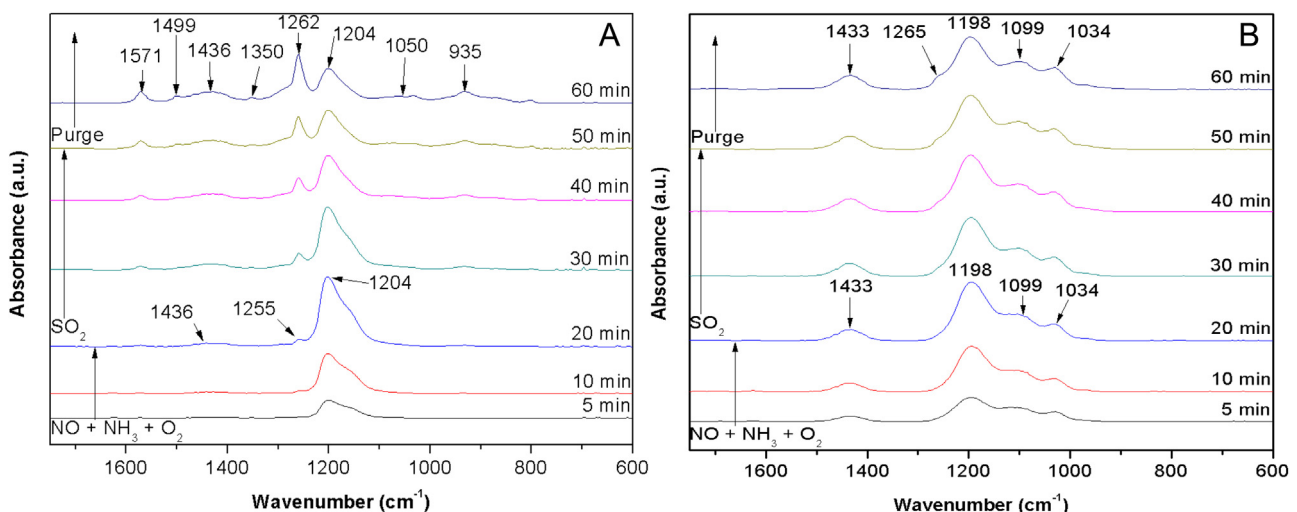


Fig. 11. *In-situ* DRIFTS of FeMnO_x and Ce(12.5), for the first 20 min the catalysts are exposed to a mixture of NO, NH₃, O₂ and N₂ (0.1%, 0.1%, 3% and balance respectively) at a total flow rate of 150 mL min⁻¹. After 20 min the gas is switched for 100 ppm SO₂ in N₂ at a total flow rate of 150 mL min⁻¹.

Mn²⁺ concentration and a decrease in Mn³⁺. A significant alteration was observed in the total Fe surface concentration, Fe²⁺ and Fe³⁺ concentrations decreased substantially during exposure to SO₂. The surface lattice oxygen was found to decline significantly and a comparable increase in chemisorbed oxygen was observed, suggesting the interaction and conversion of SO₂ at the surface of the catalyst [19]. Ce(12.5) exhibits an entirely different change to its surface after exposure to SO₂, it is found that all elements decline slightly (Tables 4 and 5), except for oxygen, which exhibits a trend similar to that found for FeMnO_x. However the reduction in lattice oxygen and subsequent increase in active oxygen is not as severe as FeMnO_x. The apparent attenuated modification of the surface as opposed to significant loss of one surface species, namely Fe²⁺ may help to explain the higher NO_x conversion exhibited by Ce(12.5) after SO₂ exposure.

3.9. In-situ DRIFTS SO₂ poisoning experiments

In-situ DRIFTS was conducted in the presence of SO₂ to further study the deactivation of FeMnO_x in comparison to the resistance exhibited by Ce(12.5) (Fig. 11). To determine the initially adsorbed species associated with the reaction, a mixture of NO, NH₃, O₂ and N₂ were flowed over the catalysts for 20 min (Figs. 11A and 11B). It can be observed that FeMnO_x (Fig. 11A) over the initial 20 min introduction of gas exhibits two major features *ca.* 1463 and 1204 cm⁻¹. On the basis of several literature sources these may be attributed to NH₄⁺ bound to Brønsted acid site and the significantly stronger of the two peaks with the formation of coordinated NH₃ on Lewis acid sites [63], a small peak appearing at 1255 cm⁻¹ is also observed, which coincides with the formation of a bridged nitrate [63]. The system was then purged with nitrogen at 120 °C and 100 ppm SO₂ was fed over the catalyst for 30 min, during this time several new peaks are observed and grow in accordance with exposure to SO₂, 935, 1050, 1262, 1350, 1436, 1499 and 1571 cm⁻¹. It is found that these features grow in tandem with significant reduction of the signal at 1204 cm⁻¹ showing that SO₂ competitively adsorbs over the catalyst and occupies sites by forming sulphate species (1262, 1050 cm⁻¹ and 935 cm⁻¹), SO₃ species (1436 cm⁻¹) and surface sulphate species with a single S=O bond (1344 cm⁻¹). HSO₄⁻(1571 cm⁻¹) [64] are also present and found to increase with SO₂ exposure time verifying the formation of an important intermediate of NH₄HSO₄. On this basis it can be suggested that the formation of NH₄SO₄ is, in part, responsible for the deactivation observed over FeMnO_x [30,34]. It is demonstrated that all species remain stable over the catalyst after purging with nitrogen for 10 min, indicating the irreversible nature of the deactivating effect of sulphur species on this catalyst. Similar positions for NH₄⁺ on Brønsted acid sites (1433 cm⁻¹) and Lewis acid coordinated NH₃ (1198 cm⁻¹) are observed over Ce(12.5) (Fig. 11B). Additional adsorbed species are also found, namely arising from *cis*-N₂O₂²⁻ (1034 cm⁻¹) and *trans*-N₂O₂²⁻ (1099 cm⁻¹) [65]. Introduction of SO₂ results in the appearance of a small shoulder (*ca.* 1265 cm⁻¹) after 30 min, indicating significant reduction of sulphate formation compared to FeMnO_x. Based upon these observations, it can be suggested that nitrogen containing species are much more stable over the Ce(12.5) catalyst compared to FeMnO_x, indicating that competitive adsorption is significantly reduced over Ce(12.5) during the timescales of this study. Similarly no signals relating to HSO₄⁻ (1571 cm⁻¹), SO₃ species (1436 cm⁻¹) or surface bound sulphate (1344 cm⁻¹) were observed, demonstrating the enhanced stability of the catalyst in the presence of SO₂. It can be determined, that the FeMnO_x catalyst exhibits significant adsorption of SO₂ which leads to irreversible deactivation caused by sulphate/sulphite formation on the surface of the catalyst, in conjunction with the formation of HSO₄⁻, an intermediate of NH₄HSO₄, which leads to gradual pore

blockage. Conversely Ce(12.5) results in very minor formation of bulk sulphate after 30 min of exposure to SO₂, demonstrating an improved resistance of the catalyst towards SO₂.

4. Conclusions

The influence of ceria addition to FeMnO_x upon low-temperature SCR catalytic activity and SO₂ resistance was examined. Catalysts containing CeO_x exhibited increased concentration of chemisorbed surface oxygen compared to FeMnO_x, in conjunction with lower NO and NH₃ adsorption, which resulted in improved turnover 2–4 times greater than FeMnO_x. This enhancement effect is attributed to the fast–SCR reaction, which is favoured by reduced NH₃ adsorption and a suitable ratio between NO sites and chemisorbed surface oxygen. Both catalysts were found to be affected via the introduction of SO₂ during SCR. However Ce(12.5) possessed significant recovery after stopping SO₂, no loss of pore volume was found, though a small loss of surface area and a general reduction of surface species occurred. Ce(12.5) possessed stable N-containing surface species, which resulted in very little metal sulphate and no obvious NH₄HSO₄ formation, leading to enhanced sulphur resistance.

Acknowledgments

This study was financially supported by the National Natural Science Foundation of China (Grant No. 21576096, 21276095) and Sinopec Corporation Commission Program (Grant No. 112022).

Appendix A. Supplementary data

Supplementary data associated with this article can be found, in the online version, at <http://dx.doi.org/10.1016/j.apcatb.2017.01.019>.

References

- [1] B. Jiang, Y. Liu, Z. Wu, J. Hazard. Mater. 162 (2009) 1249.
- [2] X. Tang, J. Hao, W. Xu, J. Li, Chin. J. Catal. 27 (2006) 843.
- [3] G. Qi, R.T. Yang, J. Catal. 217 (2003) 843.
- [4] G. Qi, R.T. Yang, R. Chang, Appl. Catal. B 51 (2004) 93.
- [5] M. Kang, E.D. Park, J.M. Kim, J.E. Yie, Appl. Catal. A 327 (2007) 261.
- [6] M. Kobayashi, R. Kuma, A. Morita, Catal. Lett. 112 (2006) 37.
- [7] R.Q. Long, R.T. Yang, R. Chang, Chem. Commun. 5 (2002) 452.
- [8] X. Tang, J. Hao, W. Xu, J. Li, Catal. Commun. 8 (2007) 329.
- [9] W.S. Kijlstra, D.S. Brands, E.K. Poels, A. Bliek, J. Catal. 171 (1997) 208.
- [10] W. Xu, H. He, Y. Yu, J. Phys. Chem. C 113 (2009) 4426.
- [11] G. Qi, R.T. Yang, Appl. Catal. B 44 (2003) 217.
- [12] S.T. Choo, S.D. Yim, I. Nam, S. Ham, J. Lee, Appl. Catal. B 44 (2003) 237.
- [13] G. Xie, Z. Liu, Z. Zhu, Q. Liu, J. Ge, Z. Huang, J. Catal. 224 (2004) 36.
- [14] W.S. Kijlstra, M. Biervliet, E.K. Poels, A. Bliek, Appl. Catal. B 16 (1998) 327.
- [15] X. Tang, J. Hao, H. Yi, J. Li, Catal. Today 126 (2007) 406.
- [16] M. Kang, E.D. Park, J.M. Kim, J.E. Yie, Catal. Today 111 (2006) 236.
- [17] Z. Wu, R. Jin, H. Wang, Y. Liu, Catal. Commun. 10 (2009) 935.
- [18] R. Ke, J. Li, X. Liang, J. Hao, Catal. Commun. 8 (2007) 2096.
- [19] F. Notoya, C. Su, E. Sasaoka, S. Nojima, Ind. Eng. Chem. Res. 40 (2001) 3732.
- [20] Z. Chen, Q. Yang, H. Li, X. Li, L. Wang, S.C. Tsang, J. Catal. 276 (2010) 56.
- [21] X. Gao, Q. Yang, H. Li, Z. Chen, X. Li, L. Wang, Chin. J. Chem. Phys. 25 (2009) 601.
- [22] J.A. Rodriguez, S. Ma, P. Liu, J. Hrbek, J. Evans, M. Perez, Science 318 (2007) 1757.
- [23] M.A. Centeno, K. Hadjiivanov, T. Venkov, H. Klimev, J.A. Odriozola, J. Mol. Catal. A 252 (2006) 142.
- [24] C. Tang, M. Kuo, C. Lin, C. Wang, S. Chien, Catal. Today 131 (2008) 520.
- [25] L. Chung, C. Yeh, Catal. Commun. 9 (2008) 670.
- [26] N.A.S. Amin, E.F. Tan, Z.A. Manan, J. Catal. 222 (2004) 100.
- [27] M. Casapu, O. Krocher, M. Elsener, Appl. Catal. B 88 (2009) 413.
- [28] H. Yan, T. Zhiqian, W. Bing, Z. Junfeng, J. Fuel Chem. Technol. 36 (2008) 616.
- [29] M. Zhang, C. Li, L. Qu, M. Fu, G. Zeng, C. Fan, J. Ma, F. Zhan, Appl. Surf. Sci. 300 (2014) 58.
- [30] D.W. Kwon, K.B. Nam, S.C. Hong, Appl. Catal. B 166 (2015) 37.
- [31] D. Mukherjee, B.G. Rao, B.M. Reddy, Appl. Catal. B 195 (2016) 105.
- [32] S. Rama, B.G. Rao, P. Venkataswamy, A. Rangaswamy, B.M. Reddy, J. Mol. Catal. A 415 (2016) 113.
- [33] B. Shen, X. Zhang, H. Ma, Y. Yao, T. Liu, J. Environ. Sci. 25 (2013) 791.

- [34] L. Zhu, Z. Zhong, H. Yang, C. Wang, Environ. Technol. (2016), <http://dx.doi.org/10.1080/09593330.2016.1226393>.
- [35] X. Gu, J. Ge, H. Zhang, A. Auoux, J. Shen, Thermochim. Acta 451 (2006) 84.
- [36] L. Shi, W. Chu, F. Qu, J. Hu, M. Li, J. Rare Earth 26 (2008) 836.
- [37] A. Mineshige, T. Taji, Y. Muroi, M. Kobune, S. Fujii, N. Nishi, M. Inaba, Z. Ogumi, Solid State Ionics 135 (2000) 481.
- [38] L.N. Ikryannikova, A.A. Aksenov, G.L. Markaryan, G.P. Murav'eva, B.G. Kostyuk, A.N. Kharlanov, E.V. Lumina, Appl. Catal. A 210 (2001) 225.
- [39] P. Venkataswamy, D. Jampaiah, K.N. Rao, B.M. Reddy, Appl. Catal. A 488 (2014) 1.
- [40] H. Bao, X. Chen, J. Fung, Z. Jiang, W. Huang, Catal. Lett. 125 (2008) 160.
- [41] X. Nie, X. Li, C. Du, Y. Huang, H. Du, J. Raman Spectrosc. 40 (2009) 76.
- [42] Z. Chen, F. Wang, H. Li, Q. Yang, L. Wang, X. Li, Ind. Eng. Chem. Res. 51 (2012) 202.
- [43] Y.N. Yang, R.L. Huang, L. Chen, J.L. Zhang, Appl. Catal. A 101 (1993) 233.
- [44] S. Paldey, S. Gedevaniashvili, W. Zhang, F. Rasouli, Appl. Catal. B 56 (2005) 241.
- [45] Y. Shen, S. Zhu, T. Qiu, S. Shen, Catal. Commun. 11 (2009) 20.
- [46] F.A. Deorsola, S. Andreoli, M. Armandi, B. Bonelli, R. Pirone, Appl. Catal. A 522 (2016) 120.
- [47] M. Salazar, S. Hoffmann, O.P. Tkachenko, R. Becker, W. Grunert, Appl. Catal. B 182 (2016) 213.
- [48] N. Yang, R. Guo, Y. Tian, W. Pan, Q. Chen, Q. Wang, C. Lu, S. Wang, Fuel 179 (2016) 305.
- [49] K.J. Lee, P.A. Kumar, M.S. Maqbool, K.N. Rao, K.H. Song, H.P. Ha, Appl. Catal. B 142–143 (2013) 705.
- [50] M. Konsolakis, Appl. Catal. B 198 (2016) 49.
- [51] L. Wei, S. Cui, H. Guo, X. Ma, L. Zhang, J. Mol. Catal. A 421 (2016) 102.
- [52] Z. Wu, R. Jin, H. Wang, Y. Liu, Catal. Commun. 10 (2009) 935.
- [53] Y. Shu, T. Aikebaier, X. Quan, S. Chen, H. Yu, Appl. Catal. B 150–151 (2014) 630.
- [54] W.S. Kijlstra, M. Biervlier, E.K. Poels, A. Bliek, Appl. Catal. B 16 (1998) 327.
- [55] R.V. Siriwardane, J.A. Poston Jr., E.P. Fisher, M.-S. Shen, A.L. Miltz, Appl. Surf. Sci. 152 (1999) 219.
- [56] X. Wu, H.-R. Lee, S. Liu, D. Weng, J. Rare Earth 30 (2012) 659.
- [57] M. Romeo, K. Bak, J.E. Fallah, F.L. Normand, L. Hilaire, Surf. Interface Anal. 20 (1993) 508.
- [58] A.M. Venezia, G. Dicarlo, L.F. Liotta, G. Melaet, N. Kruse, Appl. Catal. B 88 (2009) 430.
- [59] J. Zuo, Z. Chen, F. Wang, Y. Yu, L. Wang, X. Li, Ind. Eng. Chem. Res. 53 (2014) 2647.
- [60] Z. Wu, R. Jin, Y. Liu, H. Wang, Catal. Commun. 9 (2008) 2217.
- [61] T. Gu, Y. Liu, X. Weng, H. Wang, Z. Wu, Catal. Commun. 12 (2010) 310.
- [62] S.S.R. Putluru, L. Schill, A.D. Jensen, B. Siret, F. Tabaries, R. Fehrmann, Appl. Catal. B 165 (2015) 628.
- [63] Z. Wu, B. Jiang, Y. Liu, H. Wang, R. Jin, Environ. Sci. Technol. 41 (2007) 5812.
- [64] B.Q. Jiang, Z.B. Wu, Y. Liu, S.C. Lee, W.K. Ho, J. Phys. Chem. C 114 (2010) 4961.
- [65] L. Chen, X. Niu, Z. Li, Y. Dong, Z. Zhang, F. Yuan, Y. Zhu, Catal. Commun. 85 (2016) 48.